arXiv:1506.02599v2 [cond-mat.str-el] 22 Sep 2015

Optical properties of the perfectly compensated semimetal WTe_2

C. C. Homes,[1,*] M. N. Ali,[2] and R. J. Cava[2]

[1] *Condensed Matter Physics and Materials Science Department, Brookhaven National Laboratory, Upton, New York 11973, USA*

[2] *Department of Chemistry, Princeton University, Princeton, New Jersey 08544, USA*

(Dated: June 23, 2021; ver. 5)

The optical properties of layered tungsten ditelluride have been measured over a wide temperature and frequency range for light polarized in the *a*-*b* planes. A striking low-frequency plasma edge develops in the reflectance at low temperature where this material is a perfectly compensated semimetal. The optical conductivity is described using a two-Drude model which treats the electron and hole pockets as separate electronic subsystems. At low temperature, one scattering rate collapses by over two orders of magnitude, while the other also undergoes a significant, but less dramatic, decrease; both scattering rates appear to display the quadratic temperature dependence expected for a Fermi liquid. First principles electronic structure calculations reveal that the low-lying optical excitations are due to direct transitions between the bands associated with the electron and hole pockets.

PACS numbers: 78.30.-j, 72.15.Lh, 71.20.Be

Materials containing tellurium display a wide range of electronic properties that make them of interest for a variety of different applications, including photovoltaics [1], thermoelectrics [2], *p*-type semiconductors [3], topological insulators [4], and superconductors [5]. To add to this wide variety of phenomena it has recently been proposed that the layered transition metal dichalcogenide WTe_2 is a perfectly compensated semimetal at low temperature [6], i.e., the number of electrons and holes per unit volume is identical. A simple two-band model predicts that the magnetoresistance will saturate at high fields, unless the material is compensated, in which case the magnetoresistance will increase quadratically with field [7]. The magnetoresistance of WTe_2 increases in precisely such a fashion; moreover, it becomes extremely large at low temperature and and shows no signs of saturation, even at very high fields [6]. Electronic structure and transport studies indicate that there are electron and hole pockets in this material [8, 9], and angle resolved photoemission studies show that at low temperature they are almost exactly the same size [10, 11], resulting in a perfectly compensated semimetal. The zero-field behavior is equally dramatic with a very large residual resistivity ratio of $\rho(300\,\mathrm{K})/\rho(5\,\mathrm{K}) \simeq 300$, with $\rho(5\,\mathrm{K}) \simeq 2 \times 10^{-6}\ \Omega\,\mathrm{cm}$ [6]. It is expected that such a dramatic change in the resistivity should produce striking changes in the optical properties of this material.

In this study the optical properties of WTe_2 are determined in the *a*-*b* plane in the absence of a magnetic field over a wide frequency and temperature range. The reflectance reveals the formation of a striking low-frequency plasma edge at low temperature. The complex conductivity indicates that the electron and hole pockets give rise to carriers with dramatically different scattering rates. While both follow a quadratic temperature dependence and may be thought of as Fermi liquids, one scattering rate decreases by more than two orders of magnitude at low temperature and is responsible for the formation of a plasma edge in the reflectance. Previous electronic structure calculations are reproduced, showing electron and hole pockets of roughly equal size, and extended to include the real part of the in-plane optical conductivity. The low-energy interband transitions are shown to originate from direct transitions between the bands associated with the hole and electron pockets.

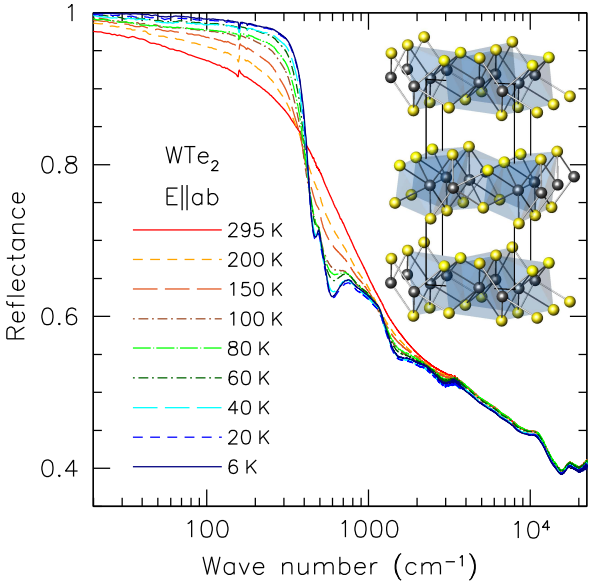

Figure 1. (Color online) The temperature dependence of the reflectance of in the infrared region of WTe_2 for light polarized in the *a*-*b* planes, revealing the formation of a sharp plasma edge in the reflectance with decreasing temperature. Inset: The unit cell is shown for the *b*-*c* face projected along the *a* axis.

Single crystals of WTe_2 were grown using a bromine

Typeset by REVTEX

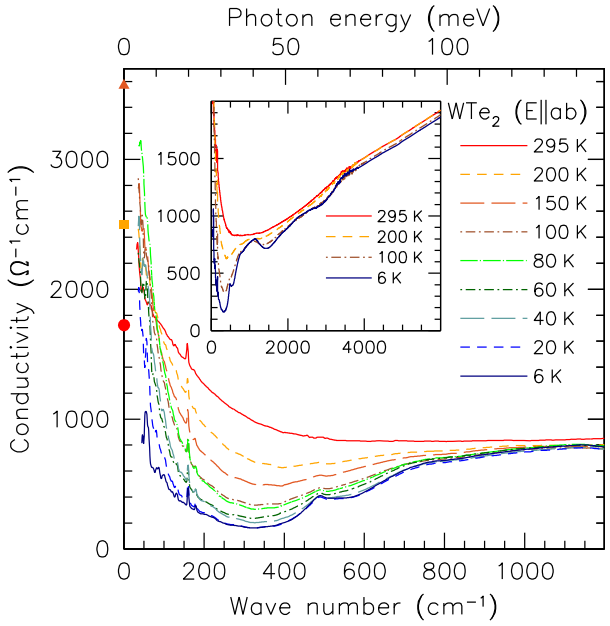

Figure 2. (Color online) The temperature dependence of the real part of the optical conductivity of WTe_2 for light polarized in the a-b planes. The symbols along the y axis denote the values for σ_{DC} obtained from transport measurements [6]. Inset: The optical conductivity for a restricted set of temperatures over a wider frequency range.

vapor transport method [6]. WTe_2 crystallizes in the orthorhombic $Pmn2_1$ space group [12], where the tungsten atoms form chains along the a axis and lie between sheets of tellurium atoms, forming the a-b planes. The sheets stack along the c axis and are easily exfoliated (inset of Fig. 1). The foil-like platelets were glued to a metal backing plate for support and then mounted on optically-black cones. The temperature dependence of the reflectance, shown in Fig. 1, was measured for light polarized in the a-b planes over a wide frequency range ($\simeq$ 2 meV to 3 eV) using an *in situ* overcoating technique [13]. The low-frequency reflectance is characteristic of a metallic response, increasing dramatically with decreasing temperature and revealing a sharp plasma edge at $\sim 300 - 400$ cm^{-1}. The optical conductivity has been determined from a Kramers-Kronig analysis of the reflectance [14], which requires that the reflectance be supplied over the entire frequency range; below the lowest measured frequency a metallic Hagen-Rubens form has been employed, $1 - R(\omega) \propto \sqrt{\omega}$, while above the highest-measured frequency the reflectance is assumed to decrease as $1/\omega$ up to 1.5×10^5 cm^{-1}, above which a free-electron $1/\omega^4$ extrapolation was used [15].

The optical conductivity in the infrared region is shown in Fig. 2. At high temperatures the response may be reasonably described by a single Drude component (a Lorentzian centered at zero frequency where the full width at half maximum is the free-carrier scattering rate), that gives way to a mid-infrared response that is dominated by interband transitions. As the temperature is reduced this Drude-like feature narrows considerably leading to a transfer of spectral weight (area under the conductivity curve) from high to low frequency, revealing several interband transitions, shown more clearly in the inset of Fig. 2. Above 2000 cm^{-1} (0.25 eV) the optical conductivity increases linearly with frequency until roughly 1 eV; we argue that this linear behavior is due to the superposition of several different interband transitions and not due to a strong renormalization of the free-carrier scattering rate [16, 17]. At high temperature there is reasonable agreement with $\sigma_1(\omega \to 0)$ and the transport values for $\sigma_{DC} = 1/\rho$. However, at low temperatures a single Drude component is not capable of describing both the extremely high values for σ_{DC} and the shape of the low-frequency conductivity. Given that there are both electron and hole pockets in this material, it is appropriate to employ a model that accounts for both types of carriers [18]. The complex dielectric function $\tilde{\epsilon} = \epsilon_1 + i\epsilon_2$ of the so-called two-Drude model is

$$\tilde{\epsilon}(\omega) = \epsilon_\infty - \sum_{j=1}^{2} \frac{\omega_{p,j}^2}{\omega^2 + i\omega/\tau_j} + \sum_k \frac{\Omega_k^2}{\omega_k^2 - \omega^2 - i\omega\gamma_k}, \quad (1)$$

where ϵ_∞ is the real part at high frequency. In the first sum $\omega_{p,j}^2 = 4\pi n_j e^2/m_j^*$ and $1/\tau_j$ are the square of the plasma frequency and scattering rate for the delocalized (Drude) carriers in the jth band, respectively, and n_j and m_j^* are the carrier concentration and effective mass. In the second summation, ω_k, γ_k and Ω_k are the position, width, and strength of the kth vibration or bound excitation. The complex conductivity is $\tilde{\sigma}(\omega) = \sigma_1 + i\sigma_2 = -2\pi i\,\omega[\tilde{\epsilon}(\omega) - \epsilon_\infty]/Z_0$, where $Z_0 \simeq 377\ \Omega$ is the impedance of free space, yielding units for the conductivity of Ω^{-1}cm^{-1}.

The two-Drude model is fit simultaneously to both σ_1 and σ_2 using a non-linear least-squares method. The fit to the data at 100 K shown in Fig. 3 indicates that the optical conductivity can be reproduced quite well using two Drude components, in addition to a series of Lorentzian oscillators at $\simeq$ 800, 1100 and 1950 cm^{-1} ($\simeq$ 100, 136 and 240 meV); other bound excitations above $\simeq$ 3500 cm^{-1} (430 meV) are also included in the total fit but not discussed. At 100 K the two Drude contributions are of roughly equal weight with $\omega_{p,1} = 3000 \pm 200$ cm^{-1}, $1/\tau_1 = 26 \pm 5$ cm^{-1} and $\omega_{p,2} = 3400 \pm 200$ cm^{-1}, $1/\tau_2 = 89 \pm 12$ cm^{-1}; fits at 80 and 150 K returned similar values for the plasma frequencies, so they have been assumed to be temperature independent and are not fitted parameters. While fitting to both scattering rates at 100 K works reasonably well, at higher temperatures the broad nature of the conductivity leads to larger values for the scattering rates and increasing uncertainties. At lower temperatures the dramatic increase

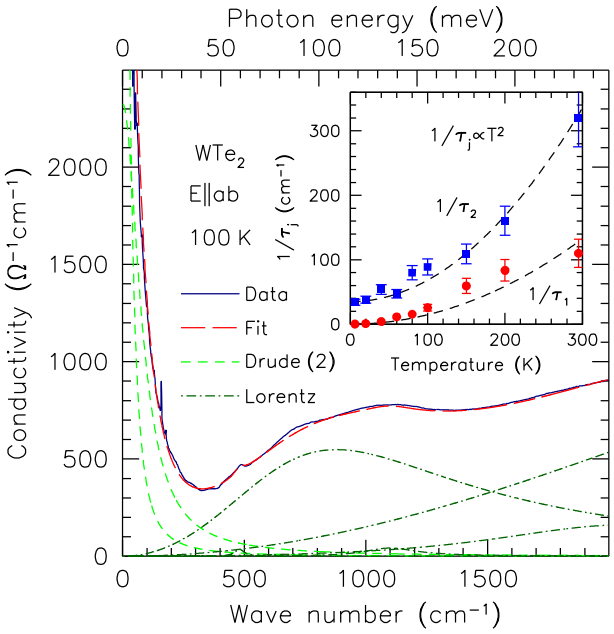

Figure 3. (Color online) The fit to the complex optical conductivity of WTe_2 at 100 K. The fit is composed of two Drude responses (dashed lines) and several Lorentzian features (dot-dash lines); the linear combination (long-dash line) reproduces the real part of the optical conductivity quite well. Inset: The fitted values for $1/\tau_1$ (circles) and $1/\tau_2$ (squares); the dashed lines are drawn as a guide to the eye.

in $\sigma_{\rm DC}$ below 100 K suggests that $1/\tau_1$ is becoming too small to be reliably determined from fits to $\tilde{\sigma}(\omega)$. In order to provide an anchor for the fits to the scattering rates, $1/\tau_1$ is first estimated from the Drude formula $1/\tau_1 = 2\pi\,\omega_{p,1}^2/(Z_0\,\sigma_0)$. For those temperatures where a direct comparison between transport and optics is possible, it appears that $\sigma_0 = \sigma_1(\omega \to 0) \simeq 1.2\,\sigma_{\rm DC}$, so we have used the approximation $\sigma_0 \simeq 1.2\,\sigma_{\rm DC}$. Treating $1/\tau_1$ as static, only $1/\tau_2$ is fit to the optical conductivity, allowing the contribution $\sigma_{02} = 2\pi\,\omega_{p,2}^2\,\tau_2/Z_0$ to be calculated where $\sigma_0 = \sigma_{01} + \sigma_{02}$; the iterative improvement in $1/\tau_1$ is determined from $1/\tau_1 = 2\pi\,\omega_{p,1}^2/(Z_0\,\sigma_{01})$. The temperature dependence of the transport values of ρ, σ_0, and the scattering rates determined in this fashion are summarized in Table I. The temperature dependence of $1/\tau_1$ and $1/\tau_2$ is shown in the inset of Fig. 3 as circles and squares, respectively. While there is some uncertainty of the scattering rates at high temperature, in both cases they follow a roughly quadratic temperature dependence, suggesting both sets of carriers resemble a Fermi liquid [19–21]. While $1/\tau_2$ decreases by roughly an order of magnitude at low temperature, it does not rival the dramatic collapse of $1/\tau_1$ from $\simeq$ 110 cm^{-1} at 295 K to $\simeq$ 0.3 cm^{-1} at 5 K, associated with the formation of the plasma edge in the reflectance. At low temperature the extremely large, non-saturating magnetoresistance indicates that this material is perfectly compensated [10],

Table I. Transport values ρ and σ_0, and optical scattering rates $1/\tau_1$ and $1/\tau_2$.

T (K)	ρ[a] ($\mu\Omega$ cm)	σ_0 ($\times 10^3\,\Omega^{-1}$cm^{-1})	$1/\tau_1$ (cm^{-1})	$1/\tau_2$ (cm^{-1})
295	580	2.07	110 ± 22	320 ± 45
200	400	3.00	84 ± 16	160 ± 22
150	280	4.28	60 ± 12	109 ± 15
100	150	8.00	26 ± 5	89 ± 12
80	100	12.0	16 ± 3	80 ± 11
60	70	17.2	12 ± 2	47 ± 6
40	30	40.0	4.1 ± 0.8	54 ± 7
20	7	171	0.90 ± 0.2	38 ± 5
6	2	600	0.25 ± 0.05	34 ± 4

[a] Ref. 6

i.e. $n_1 = n_2$. From the values of $\omega_{p,1}$ and $\omega_{p,2}$, it may be shown that carrier masses are similar, $m_2 \simeq 0.8 m_1$, in good agreement with Shubnikov-de-Hass oscillation measurements [22].

There are a series of excitations in the infrared at $\simeq 100, 136$ and 240 meV, as well as several others above 0.4 eV; these absorptions are in general quite broad and have a substantial amount of spectral weight at low frequency. Previous band structure studies of WTe_2 revealed a semimetallic character with small electron and hole pockets [6, 9]; these results have been reproduced and extended in this work (the details of the calculations [23–25] are discussed in the supplementary materials).

The calculated electronic band structure including the effects of spin-orbit coupling is shown in Fig. 4(a) for paths between several different high-symmetry points in the orthorhombic Brillouin zone, revealing both electron and hole bands in the $\Gamma - X$ direction, in good agreement with previous results [6, 9]. A more detailed examination of the band structure, (supplementary material), reveals several bands that lie just above and below the Fermi level $\epsilon_{\rm F}$ that may be responsible for the low-energy interband transitions. To explore this further the total density of states (DOS) for the W and Te atoms is calculated using a fine k-point mesh (10 000 k points) and shown in Fig. 4(b). The low value for the DOS at $\epsilon_{\rm F}$ is consistent with the semimetallic nature of this material. The prominent increase in the DOS in the $200 - 500$ meV above $\epsilon_{\rm F}$ is larger than $50 - 150$ meV interval over which interband transitions are observed in the optical conductivity. However, the optical conductivity is a reflection of the joint density of states (JDOS) rather than just the DOS. The real part of the optical conductivity has been calculated [26] using the same fine k-point mesh for $\sigma_{x,x}$ and $\sigma_{y,y}$ (a and b axes, respectively), shown in Fig. 4(c), and is compared to the experimental value for the conductivity at 5 K with the Drude contributions removed. Both $\sigma_{x,x}$ and $\sigma_{y,y}$ have a very weak absorption at about 25 meV with the onset of much stronger absorptions occurring above about 50 meV, with $\sigma_{x,x}$ dis-

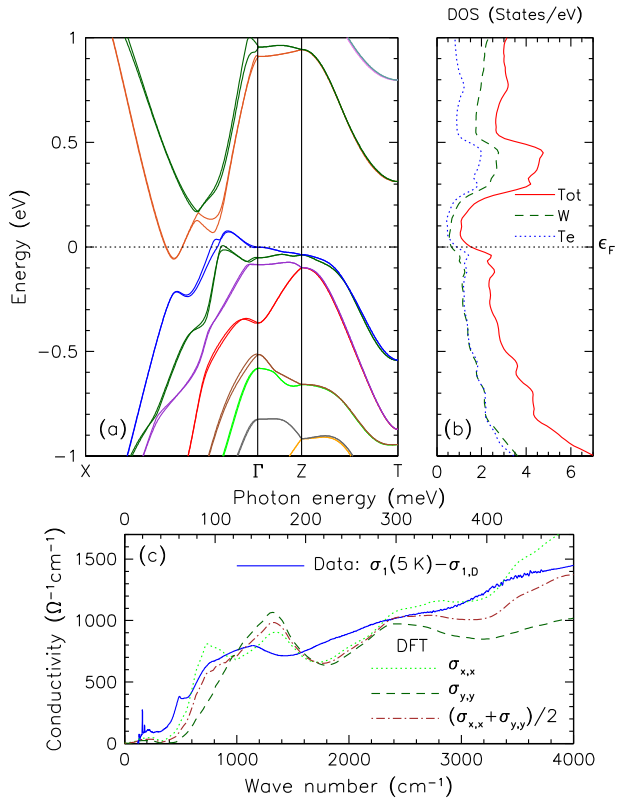

Figure 4. (Color online) (a) The calculated electronic structure WTe_2 including the effects of spin-orbit coupling between several different high symmetry points of the orthorhombic Brillouin zone. (b) The total density of states (DOS), including the contributions from the W and Te atoms. (c) The real part of the calculated optical conductivity $\sigma_{x,x}$, $\sigma_{y,y}$ and average of the two, compared to the measured optical conductivity at 5 K with the Drude terms removed.

playing prominent features at $\simeq$ 80 and 160 meV, while only the 160 meV peak is present $\sigma_{y,y}$; above $\simeq$ 200 meV the two conductivities continue to increase steadily with frequency. The average of the two curves reproduces the experimental data reasonably well. The details of the contributions to the optical conductivity, (supplementary material), reveal that these two strong absorptions at 80 and 160 meV originate from direct transitions between the bands associated with the hole and electron pockets. The feature at 60 meV, which occurs at too high an energy to be a lattice vibration [27], remains unexplained; however, it has been shown that there are very low-energy excitations in this material. Because this feature only emerges at low temperature where the material is perfectly compensated, it is likely that it is due to a low-energy interband transition that is sensitive upon the details of the band structure that may not captured in this calculation.

To conclude, the complex optical properties of the perfectly compensated semimetal WTe_2 have been measured in the a-b planes for a variety of temperatures over a wide frequency range. The electron and hole pockets are described using the two-Drude model, revealing that as the temperature is reduced one scattering rate collapses by over two orders of magnitude, resulting in the formation of a striking plasma edge in the reflectance, while the other scattering rate is considerably larger and does not decrease by nearly the same amount. Both sets of carriers may be described as Fermi liquids. The calculated optical conductivity indicates that low-energy absorptions are due to direct transitions between the bands associated with the hole and electron pockets. The emergence of a narrow low-energy absorption at low temperature is thought to be a low-lying interband transition related to subtle changes in the electronic structure that result in a perfectly compensated semimetal.

We would like to acknowledge illuminating discussions with T. Valla. This work is supported by the Office of Science, U.S. Department of Energy under Contract No. DE-SC0012704 and by the Army Research Office, grant W911NF-12-1-0461.

* homes@bnl.gov

[1] B. M. Basol and B. McCandless, J. Photon. Energy. **4**, 040996 (2014).
[2] H. J. Goldsmid, Materials **7**, 2577 (2015).
[3] K. E. Petersen, U. Birkholz, and D. Adler, Phys. Rev. B **8**, 1453 (1973).
[4] X.-L. Qi and S.-C. Zhang, Rev. Mod. Phys. **83**, 1057 (2011).
[5] T. J. Liu, J. Hu, B. Qian, D. Fobes, Z. Q. Mao, W. Bao, M. Reehuis, S. A. J. Kimber, K. Prokeš, S. Matas, D. N. Argyriou, A. Hiess, A. Rotaru, H. Pham, L. Spinu, Y. Qiu, V. Thampy, A. T. Savici, J. A. Rodriguez, and C. Broholm, Nature Mater. **9**, 718 (2010).
[6] M. N. Ali, J. Xiong, S. Flynn, J. Tao, Q. D. Gibson, L. M. Schoop, T. Liang, N. Haldolaarachchige, M. Hirschberger, N. P. Ong, and R. J. Cava, Nature (London) **514**, 205208 (2014).
[7] E. Fawcett and W. A. Reed, Phys. Rev. **131**, 2463 (1963).
[8] S. Kabashima, J. Phys. Soc. Jpn. **21**, 945 (1966).
[9] J. Augustin, V. Eyert, T. Böker, W. Frentrup, H. Dwelk, C. Janowitz, and R. Manzke, Phys. Rev. B **62**, 10812 (2000).
[10] I. Pletikosić, M. N. Ali, A. V. Fedorov, R. J. Cava, and T. Valla, Phys. Rev. Lett. **113**, 216601 (2014).
[11] J. Jiang, F. Tang, X. C. Pan, H. M. Liu, X. H. Niu, Y. X. Wang, D. F. Xu, H. F. Yang, B. P. Xie, F. Q. Song, X. G. Wan, and D. L. Feng, arXiv:1503.01422 [cond-mat].
[12] A. Mar, S. Jobic, and J. A. Ibers, J. Am. Chem. Soc. **114**, 8963 (1992).
[13] C. C. Homes, M. Reedyk, D. A. Crandles, and T. Timusk, Appl. Opt. **32**, 2976 (1993).
[14] M. Dressel and G. Grüner, *Electrodynamics of Solids* (Cambridge University Press, Cambridge, 2001).
[15] F. Wooten, *Optical Properties of Solids* (Academic Press, New York, 1972) pp. 244–250.
[16] J. W. Allen and J. C. Mikkelsen, Phys. Rev. B **15**, 2952 (1977).

[17] A. Puchkov, D. N. Basov, and T. Timusk, J. Phys.: Condens. Matter **8**, 10049 (1996).
[18] D. Wu, N. Barišić, P. Kallina, A. Faridian, B. Gorshunov, N. Drichko, L. J. Li, X. Lin, G. H. Cao, Z. A. Xu, N. L. Wang, and M. Dressel, Phys. Rev. B **81**, 100512(R) (2010).
[19] R. N. Gurzhi, Sov. Phys. JETP **8**, 673 (1959).
[20] D. L. Maslov and A. V. Chubukov, Phys. Rev. B **86**, 155137 (2012).
[21] C. Berthod, J. Mravlje, X. Deng, R. Žitko, D. van der Marel, and A. Georges, Phys. Rev. B **87**, 115109 (2013).
[22] P. L. Cai, J. Hu, L. P. He, J. Pan, X. C. Hong, Z. Zhang, J. Zhang, J. Wei, Z. Q. Mao, and S. Y. Li, Phys. Rev. Lett. **115**, 057202 (2015).
[23] D. J. Singh, *Planewaves, Pseudopotentials and the LAPW method* (Kluwer Adademic, Boston, 1994).
[24] D. Singh, Phys. Rev. B **43**, 6388 (1991).
[25] P. Blaha, K. Schwarz, G. K. H. Madsen, D. Kvasnicka and J. Luitz, WIEN2k, *An augmented plane wave plus local orbitals program for calculating crystal properties* (Techn. Universität Wien, Austria, 2001).
[26] C. Ambrosch-Draxl and J. O. Sofo, Comp. Phys. Commun. **175**, 1 (2006).
[27] W.-D. Kong, S.-F. Wu, P. Richard, C.-S. Lian, J.-T. Wang, C.-L. Yang, Y.-G. Shi, and H. Ding, Appl. Phys. Lett. **106**, 081906 (2015).

Supplementary material for Optical properties of the perfectly compensated semimetal WTe_2

C. C. Homes,[1,*] M. N. Ali,[2] and R. J. Cava[2]

[1] *Condensed Matter Physics and Materials Science Department, Brookhaven National Laboratory, Upton, New York 11973, USA*

[2] *Department of Chemistry, Princeton University, Princeton, New Jersey 08544, USA*

(Dated: September 9, 2015)

ELECTRONIC STRUCTURE CALCULATIONS

Tungsten ditelluride, WTe_2, crystallizes in the orthorhombic $Pmn2_1$ space group [1], where the tungsten atoms form chains along the a axis and lie between sheets of tellurium atoms, forming the a-b planes; the unit cell is reproduced from the main text in Fig. S1 for convenience. The electronic structure of WTe_2 was calculated using both the local spin density approximation (LSDA) as well as the generalized gradient approximation (GGA) using the full-potential linearized augmented plane-wave (FP-LAPW) method [2] with local-orbital extensions [3] in the WIEN2k implementation [4]. The system was assumed to be non-magnetic. An examination of different Monkhorst-Pack k-point meshes indicated that a $9 \times 5 \times 2$ mesh and $R_{mt}k_{max} = 7.75$ was sufficient for good energy convergence. The geometry of the unit cell was refined through an iterative process whereby the volume was optimized with respect to the total energy while the c/a ratio remained fixed. The atomic fractional coordinates were then relaxed with respect to the total force, typically resulting in residual forces of less than 0.2 mRy/a.u. For both of these procedures spin-orbit coupling is ignored. This approach was repeated until no further improvement was obtained. A comparison of the experimental and calculated (relaxed) unit cell parameters are shown in Table. I.

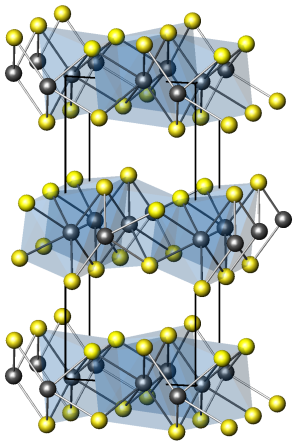

Figure S1. (Color online) The unit cell is shown for the b-c face projected along the a axis. The tungsten atoms are surrounded by tellurium octahedra that are distorted due to the zig-zag nature of the tungsten chains.

The electronic band structure has been calculated with LSDA and spin-orbit coupling for several different paths between high-symmetry points in the orthorhombic unit cell, shown in Fig. S2. This calculation accurately reproduces the work of Ali *et al.* [5], as well as an earlier work [6]. The relatively small number of bands crossing the Fermi level (ϵ_F) illustrates the semimetallic character of WTe_2. In particular, there is an electron-like band and a hole-like band crossing Fermi surface along the $\Gamma - X$ direction. Figure S2 also reveals that there are several other points in the Brillouin zone at which hole and electron bands just manage to cross the Fermi surface; however, the electronic structure is quite sensitive to the unit cell geometry, and that even a small increase (or decrease) in the Fermi level might move these bands above or below ϵ_F. While the paths along the high-symmetry directions are useful, the contributions of the hole and electron bands to the transport is best understood

Table I. The experimental and theoretical lattice constants and atomic fractional coordinates for the relaxed structure of WTe_2 in the orthorhombic $Pmn2_1$ space group.

	Experiment[a]		Theory (LSDA)		Theory (GGA)	
a(Å)	3.5306		3.4657		3.5423	
b(Å)	6.3443		6.2274		6.3653	
c(Å)	14.2123		13.9509		14.2595	
W1 ($\frac{1}{2}xy$)	0.39890	0.50030	0.39866	0.50076	0.39859	0.50039
W2 ($0xy$)	0.04310	0.48490	0.04368	0.48491	0.04393	0.48502
Te1 ($\frac{1}{2}xy$)	0.79410	0.59540	0.79507	0.59548	0.79470	0.59428
Te1 ($0xy$)	0.30040	0.63990	0.29920	0.64169	0.30052	0.63948
Te1 ($0xy$)	0.85620	0.84510	0.85526	0.84396	0.85649	0.84588
Te1 ($\frac{1}{2}xy$)	0.35180	0.89020	0.35271	0.89030	0.35225	0.89129

[a] Ref. 1.

Typeset by REVTEX

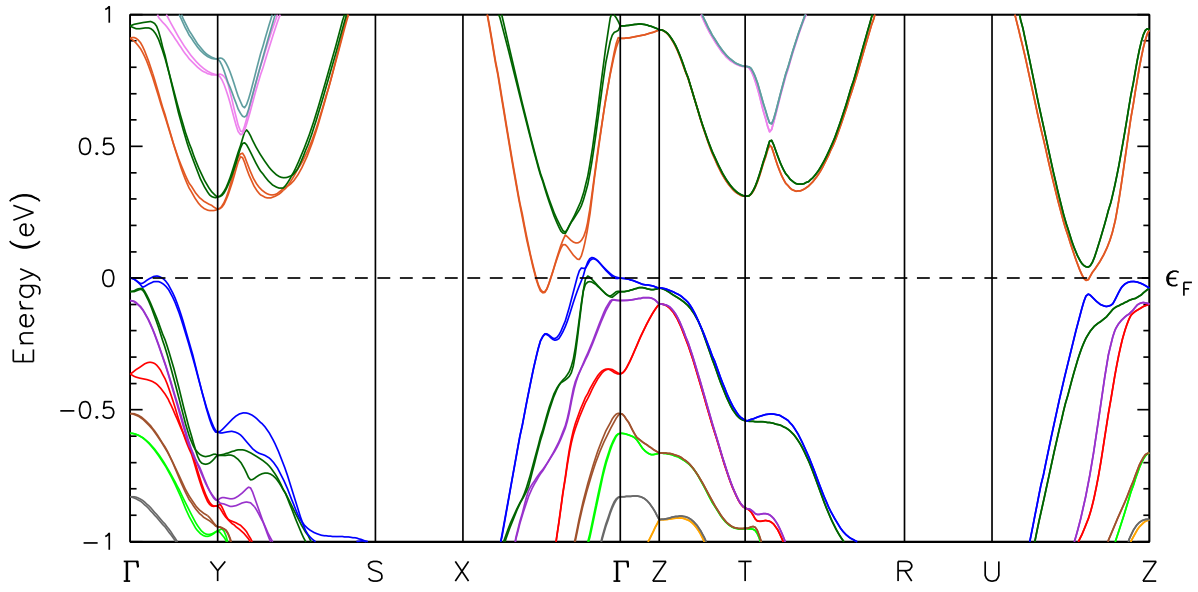

Figure S2. (Color online) The calculated LSDA electronic band structure of WTe_2 including the effects of spin-orbit coupling shown for several different paths between high-symmetry points for an orthorhombic Brillouin zone (generated using 500 k points).

from the nature of the Fermi surface.

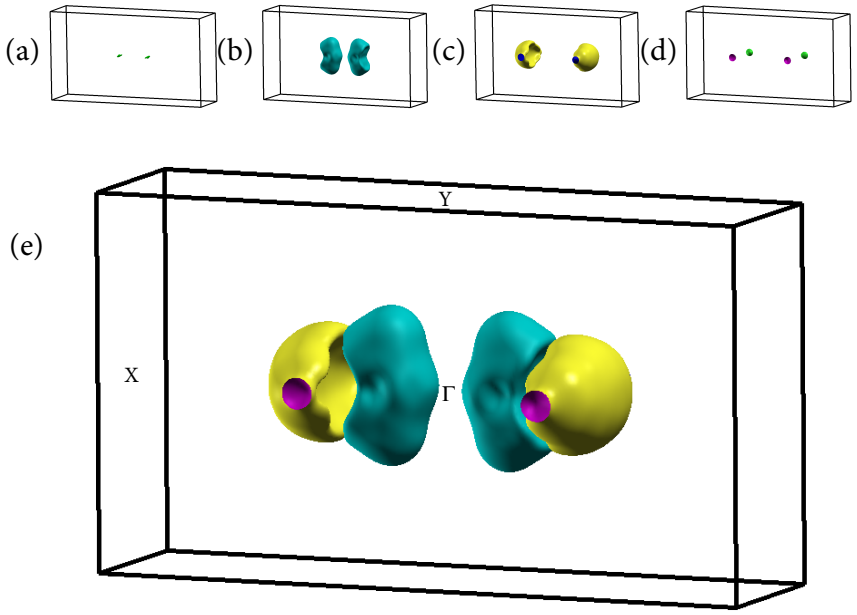

Figure S3. (Color online) The (a) small and (b) large hole LSDA Fermi surfaces. (c) Large and (d) small electron Fermi surfaces. (e) The merged Fermi surface of the electron (yellow) and hole (blue) pockets in the orthorhombic Brillouin zone along the $\Gamma - X$ direction.

FERMI SURFACE

The Fermi surface has been calculated using LSDA and a dense k-point mesh (10 000 k points, resulting in a $41 \times 23 \times 10$ mesh)[7]. The resulting Fermi surface is shown in Fig. S3 and consists of a total of four pockets; two hole pockets, one small and one large, shown in Figs. S3(a) and (b), respectively, and two electron pockets, one large and one small, shown in Figs. S3(c) and (d), respectively. The merged Fermi surface shown in Fig. S3(e) consists of the electron (yellow) and hole (blue) pockets slightly displaced from the origin of the Brillouin zone along the $\Gamma - X$ direction, in agreement with a previous calculation [5] and several experimental observations [8, 9].

DIELECTRIC TENSOR

In the main text the real part of the optical conductivity has been calculated [10] from the the imaginary part of the dielectric function, $\sigma_{x,x} = 2\pi\omega\, \Im\, \epsilon_{x,x}/Z_0$, using a fine k point mesh (10 000 k points, yielding a $41 \times 23 \times 10$ mesh); $Z_0 \approx 377\,\Omega$ is the impedance of free space, resulting the units for the conductivity of $\Omega^{-1}\text{cm}^{-1}$.

In this case, the free-carrier contribution is not calculated, so that the imaginary part of the dielectric function is the sum of the contributions to the dielectric tensor over all the allowed interband transitions. There are a total of 617 energy bands, with the last occupied band occurring at 276. Only direct ($\mathbf{q} = 0$) transitions are considered from occupied to unoccupied states; this being the case, the bands near the Fermi surface will be of particular importance as they will make the most significant contributions to the imaginary part of the dielectric function and thus the optical conductivity. The energy bands within 1 eV of the Fermi level along the $\Gamma - X$ direction have been labeled in Fig S4. Note that in the main text both $\sigma_{x,x}$ and $\sigma_{y,y}$ have been calculated; however, whereas $\sigma_{x,x}$ displays prominent structures at 650 cm^{-1} (80 meV) and 1300 cm^{-1} (160 meV), the first prominent feature in $\sigma_{y,y}$ only occurs at about 1300 cm^{-1}, therefore this calculation will focus on the result for imaginary part of $\epsilon_{x,x}$ [11]. Transitions between all energy bands have calculated; however, we will only consider contributions to $\Im\, \epsilon_{x,x} \gtrsim 0.5$. These transitions are shown in Fig. S5. For bands 235 and 236, there are only weak contributions from transitions to bands 241 and 242 that only occur at energies above about 3400 cm^{-1} (420 meV); however, for bands 237 and 238, we see contributions from an increasing number of bands (239 $\rightarrow$ 244) with a much lower onset of about 400 cm^{-1} (50 meV) with noticeable peaks at about 700 (87 meV) and 2500 cm^{-1} (310 meV). The contribution from band 239 is particulary interesting as there is an unusually low-energy transition at about 150 cm^{-1} (19 meV) with another prominent absorption at 1400 cm^{-1} (174 meV); for band 240 the strongest absorption is at about 800 cm^{-1} (99 meV). For bands 241 and 242, the remaining contributions are fairly small. Thus, the two strongest contributions are from the transitions 239 $\rightarrow$ 242 and 240 $\rightarrow$ 241, which are the energy bands related to the electron and hole pockets that form the Fermi surface so we may conclude that the low-energy interband transitions originate from these energy bands.

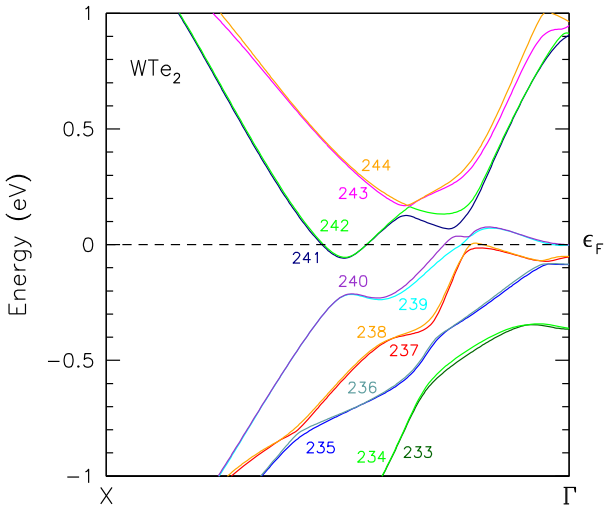

Figure S4. (Color online) The indexed LSDA energy bands near the Fermi level along the $\Gamma - X$ direction in the orthorhombic Brillouin zone.

The sum of all of the contributions to the imaginary part of the complex dielectric function $\Im\, \epsilon_{x,x}$ is shown in Fig. S6, with the calculated real part of the optical conductivity shown in the inset [note this is same quantity that is shown in Fig. 4(c)]. The peak at about 150 cm^{-1}, while prominent in the imaginary part of $\epsilon_{x,x}$, is diminished in the optical conductivity due to the effects of frequency scaling.

* homes@bnl.gov

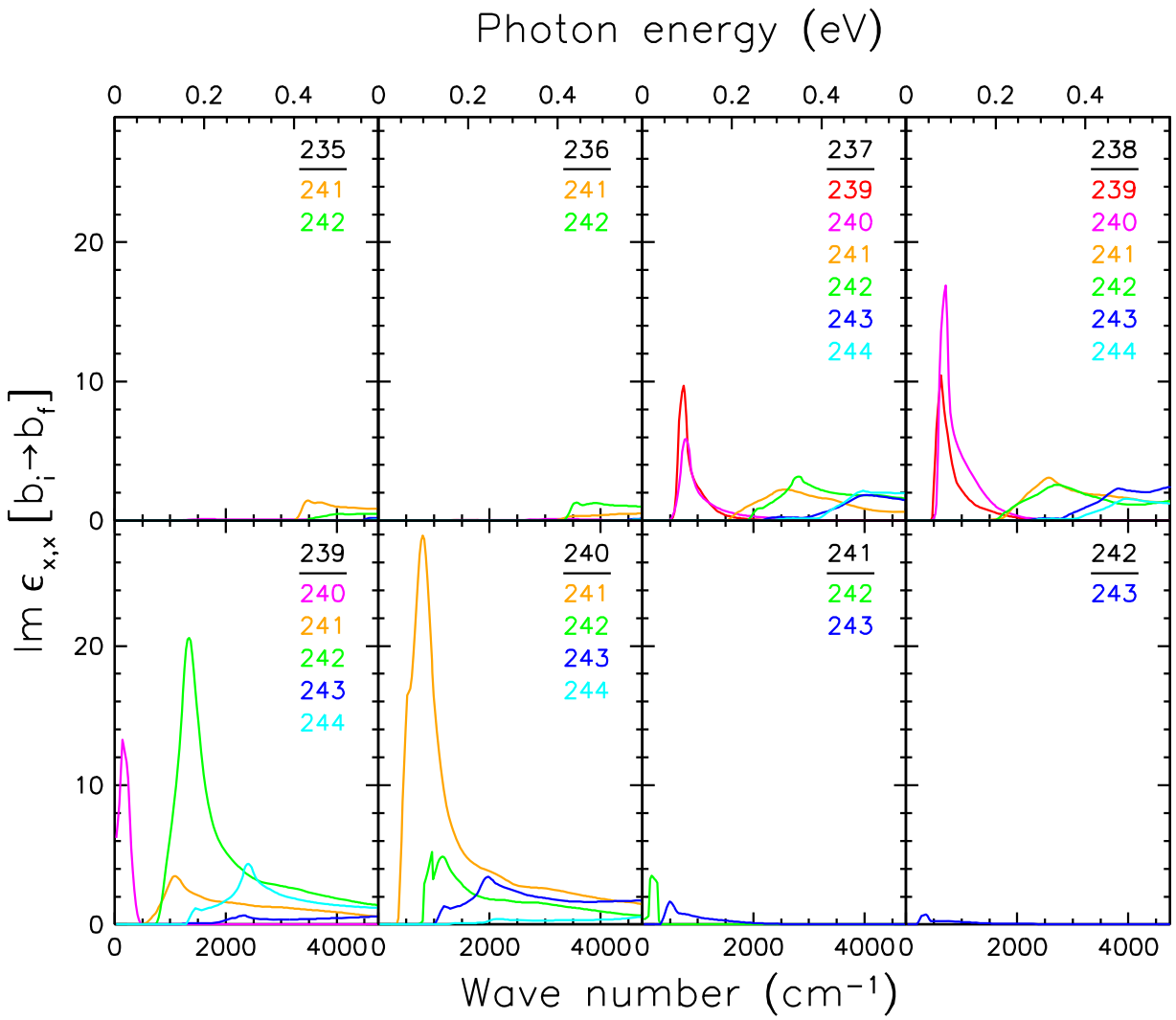

Figure S5. (Color online) The LSDA contributions to the imaginary part of the dielectric function $\Im\epsilon_{x,x}$ for the various transitions between occupied (b_i) to unoccupied (b_f) bands, beginning at 235 and ending at 242. In each panel, the initial band is above the horizontal line, while the final band (or bands) is listed below the line; note that the choice of bands was determined from the criteria at the contribution should be larger than $\simeq 0.5$.

[1] A. Mar, S. Jobic, and J. A. Ibers, "Metal-metal vs tellurium-tellurium bonding in WTe_2 and its ternary variants $TaIrTe_2$ and $NbIrTe_4$," J. Am. Chem. Soc. **114**, 8963–8971 (1992).

[2] D. J. Singh, *Planewaves, Pseudopotentials and the LAPW method* (Kluwer Adademic, Boston, 1994).

[3] David Singh, "Ground-state properties of lanthanum: Treatment of extended-core states," Phys. Rev. B **43**, 6388–6392 (1991).

[4] P. Blaha, K. Schwarz, G. K. H. Madsen, D. Kvasnicka and J. Luitz, WIEN2k, *An augmented plane wave plus local orbitals program for calculating crystal properties* (Techn. Universität Wien, Austria, 2001).

[5] Mazhar N. Ali, Jun Xiong, Steven Flynn, Jing Tao, Quinn D. Gibson, Leslie M. Schoop, Tian Liang, Neel Haldolaarachchige, Max Hirschberger, N. P. Ong, and R. J. Cava, "Large, non-saturating magnetoresistance in WTe_2," Nature (London) **514**, 205208 (2014).

[6] J. Augustin, V. Eyert, Th. Böker, W. Frentrup, H. Dwelk, C. Janowitz, and R. Manzke, "Electronic band structure of the layered compound Td – WTe_2," Phys. Rev. B **62**, 10812–10823 (2000).

[7] Anton Kokalj, "Computer graphics and graphical user interfaces as tools in simulations of matter at the atomic scale," Comp. Mat. Sci. **28**, 155–168 (2003).

[8] I. Pletikosić, Mazhar N. Ali, A. V. Fedorov, R. J. Cava, and T. Valla, "Electronic Structure Basis for the Extraordinary Magnetoresistance in WTe_2," Phys. Rev. Lett. **113**, 216601 (2014).

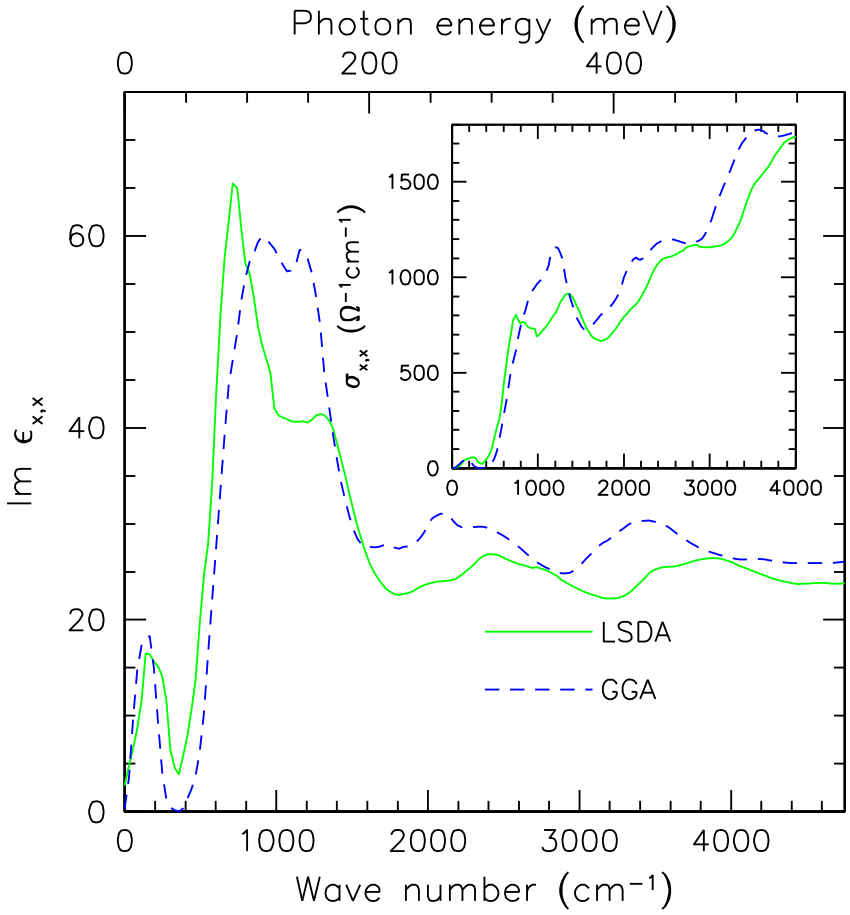

Figure S6. (Color online) The imaginary part of the dielectric function $\epsilon_{x,x}$ from a summation of all of the individual interband contributions, determined using LSDA (solid line) and GGA (dashed line) with spin-orbit coupling. Inset: The real part of the optical conductivity $\sigma_{x,x}$ calculated from the imaginary part of complex dielectric function $\epsilon_{x,x}$ using LSDA (solid line) and GGA (dashed line).

[9] J. Jiang, F. Tang, X. C. Pan, H. M. Liu, X. H. Niu, Y. X. Wang, D. F. Xu, H. F. Yang, B. P. Xie, F. Q. Song, X. G. Wan, and D. L. Feng, "Signature of strong spin-orbital coupling in the large non-saturating magnetoresistance material WTe_2," arXiv:1503.01422 [cond-mat].

[10] Claudia Ambrosch-Draxl and Jorge O. Sofo, "Linear optical properties of solids within the full-potential linearized augmented planewave method," Comp. Phys. Commun. **175**, 1–14 (2006).

[11] It is convenient to recall that $1\,\mathrm{eV} = 8065.5\,\mathrm{cm}^{-1}$.